

Influence of MgO codoping on the optical properties of Er³⁺-doped near-stoichiometric LiNbO₃

A.-H. Li · Z.-R. Zheng · T.-Q. Lü · L. Sun · W.-L. Liu ·
W.-Z. Wu

Received: 8 April 2009 / Revised version: 2 July 2009 / Published online: 7 August 2009
© Springer-Verlag 2009

Abstract Four near-stoichiometric lithium niobate (NSLN) crystals codoped with Er³⁺ (1 mol%) and MgO (0, 0.5, 1.0, and 2.0 mol%) were grown from K₂O-based flux in air using top seeded solution growth technique. The [Li]/[Nb] ratio, estimated from the blueshift of ultraviolet absorption edge, is 97.2% in NSLN:Er, MgO; codoping can increase the segregation coefficient of Er³⁺ in NSLN:Er:MgO crystal. The photorefractive damage threshold is enhanced by three orders of magnitude for NSLN:Er codoped with 1 mol% MgO, it coincides with the peak shift of OH⁻ absorption spectrum from 3481 to 3535 cm⁻¹. Judd–Ofelt theory based on absorption spectra is used to analyze the influence of MgO concentration on the Judd–Ofelt intensity parameter, transition strength, fluorescence branching ratio, and stimulated emission cross section. From the time-resolved emission spectra and the comparison among emission spectra, two Er³⁺ crystal-field sites are ascertained in NSLN:Er codoped with 2 mol% MgO, this coincides with the bimodal structure in X-ray photoelectron spectrometry spectra. The upconversion processes under pulse excitation is proposed based on the pump energy dependence and decay kinetics. The distribution of Er³⁺-clustered sites in NSLN:Er:MgO series is discussed based on the nonexponential decay curves monitored at 550 nm under two-photon excitation.

PACS 31.72.-y · 81.40.Tv · 42.65.Ky · 42.62.Fi

A.-H. Li · Z.-R. Zheng (✉) · T.-Q. Lü · W.-L. Liu · W.-Z. Wu
Center for Condensed Matter Science and Technology,
Department of Physics, Harbin Institute of Technology,
Harbin 150001, P.R. China
e-mail: zrzheng@hit.edu.cn

L. Sun
School of Material Science and Engineering, Harbin Institute
of Technology, Harbin 150001, P.R. China

1 Introduction

Ferroelectric lithium niobate (LiNbO₃, LN) crystal is an excellent material exhibiting diverse physical properties. Because of its remarkable electro-optic, ferroelectric, piezoelectric, and nonlinear optical properties, LN is applied to electro-optic modulators [1], ferroelectric random access memories (Fe-RAMs) [2], surface acoustic wave devices [3], optical frequency converters [4], and so on. Nowadays, LN is the only optical material with a degree of development and so extensively investigated to serve as the basis for the development of integrated optics playing a similar role as Si has done in the development of integrated electronics [5]. Dopant with small amount in this crystal can bring significant change to its physical properties. For example, Mg, Zn, In, Sc, and Hf dopants above certain threshold values can increase photorefractive damage threshold by more than hundred times [6–10]; and Er³⁺, Ho³⁺, Nd³⁺, and Yb³⁺ dopants can lead to lasing action in the visible and infrared (IR) regions [11, 12]. Most works are dedicated to the properties of congruent LN (CLN), which is Li deficient ([Li]/[Nb] = 0.946). In recent years it has been realized that LN crystal with stoichiometric composition has superior properties compared with CLN. Laser damage and photorefractive damage thresholds of stoichiometric or near-stoichiometric lithium niobate (SLN or NSLN) crystal are enhanced at much lower doping level compared with CLN, which is a positive factor in producing high optical quality crystal. For example, 1 mol% MgO doping is enough to improve the photorefractive damage resistance [13]. It is increasingly realized that SLN crystal is emerging as an alternative to CLN due to the advance in crystal growth technology.

For practical application, such as waveguide amplifier at 1.54 μm and intra-cavity frequency doubling, the spectro-

scopic properties of NSLN:Er:MgO are needed due to the influences of [Li]/[Nb] ratio and dopant concentration [14, 15]. While Judd–Ofelt (JO) theory is the only successful theory in quantitatively predicting the spectroscopic properties of rare earth ions [16, 17], based on JO analysis, some useful information, such as stimulated emission cross section and fluorescence branching ratio, can be obtained [18]. In addition, the decay behavior of the green upconversion fluorescence is sensitive to the clustered sites [19], which have deleterious effects on laser and amplifier at 1.54 μm .

In recent work, we have used JO theory and spectral- and time-resolved emission spectra to investigate the influence of MgO codoping on the spectroscopic properties of Er³⁺ in CLN crystals [20, 21]. In present work, we investigate the influence of MgO codoping on Er³⁺ segregation coefficient, photorefractive damage threshold, JO intensity parameter, and the distribution of Er³⁺-clustered sites in NSLN:Er:MgO crystals.

2 Experimental details

The details of crystal growth can be found elsewhere [22]. Briefly, NSLN crystals were grown along the ferroelectric *c*-axis in air using top seeded solution growth technique with K₂O as flux. Typical growth conditions were 0.15 mm/h pulling rate and 16.7 rpm rotating rate. The charges for four crystals are listed in Table 1. Crack-free boules were grown in 20–25 mm diameter and 30–35 mm length. The samples for testing were cut to *c*-oriented slices from the middle of the boules and then polished to optical grade.

X-ray photoelectron spectrometry (XPS) spectra were measured with 400- μm beam spot using a *K*-Alpha X-ray photoelectron spectrometer (Thermo Fisher Scientific Co. Ltd.). For studying photorefractive damage threshold behavior, a continuous wave (CW) frequency-doubled Nd:yttrium aluminum garnet (YAG) laser was used. The laser beam with diameter of 1.5 mm was focused onto the sample surface using a 30-cm converging lens. After passing through the sample, the laser beam profile projected on a screen was photographed. The IR transmittance was measured by a Fourier IR spectrometer (Nicolet-710, Nicolet, USA).

Optical absorption experiments were performed with unpolarized light and sample oriented in such a manner that the light beam propagated perpendicularly to the optical (*c*) axis of the crystal on a Perkin-Elmer Lambda 900 spectrophotometer. A regeneratively amplified Ti:sapphire mode-locked femtosecond laser (Spectra-Physics, Spitfire) operating at 800 nm with 1-kHz repetition rate and \sim 130-fs pulse duration was used as an excitation source. The laser beam was loosely focused onto the samples. The sample was excited at a very edge position and side fluorescence was collected from the same edge in a direction normal to the

excitation beam. The luminescence was collected by a fiber probe whose other end was connected with the entrance port of a grating spectrograph (Bruker Chromex 250IS/SM). The spectrograph output was detected by a thermoelectrically cooled intensified charge-coupled device (ICCD) detector (Andor i Star DH720). In the lifetime measurement, the laser was operated at 83 Hz with pump energy of 120 $\mu\text{J}/\text{pulse}$. Power dependency was measured using a continuously adjustable neutral density filter at a fixed focused point. All the measurements were performed at room temperature.

3 Experimental results and discussion

3.1 The composition of the as-grown NSLN:Er:MgO crystals

Dravecz et al. have demonstrated that LN grown from alkali metal oxide-based flux have low crystallization temperature and can make crystal closer to the stoichiometric composition [23]. The composition of LN can be estimated using the ultraviolet (UV) absorption edge [24]. Absorption coefficients corrected for reflection losses, which is defined by (1) of [24], are plotted in Fig. 1. Here the curve of a CLN:Er is also presented for comparison. Because our measurements are unpolarized, the blueshift (7 nm) of UV absorption edge compared with CLN instead of its position is used to calculate *c*_{Li} (refer to [24]), which is 49.3 mol% in NSLN:Er. The smaller blueshift compared with that reported in [25] (10 nm) also indicates *c*_{Li} less than 49.7 % in our crystal. Here, all NSLN crystals are assumed to own the same [Li]/[Nb] ratio. The lower [Li]/[Nb] ratio ascribes to lower K₂O content in our charges. But off-stoichiometric composition facilitates to insure the optical quality and homogeneity of the as-grown crystals.

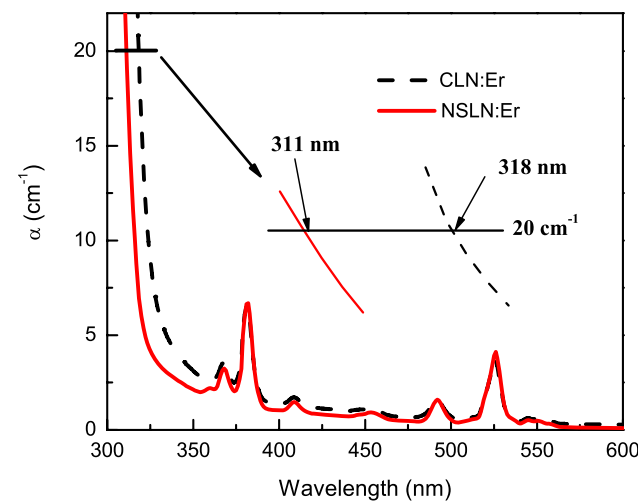


Fig. 1 Absorption coefficients corrected for reflection losses based on unpolarized absorption spectra. Inset shows the positions of UV absorption edges of CLN:Er and NSLN:Er at $\alpha = 20 \text{ cm}^{-1}$

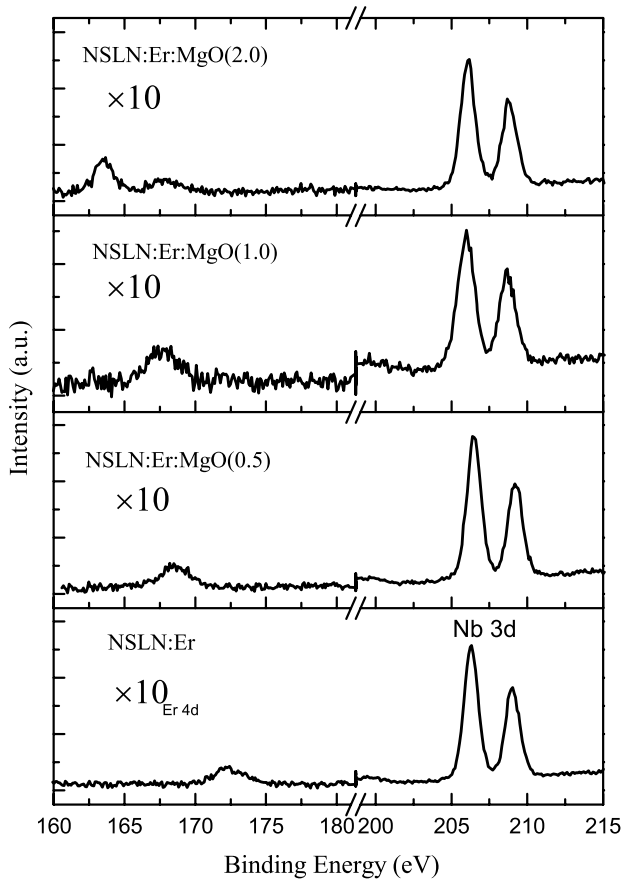


Fig. 2 Er 4d and Nb 3d binding energy of NSLN:Er:MgO crystals. All XPS spectra were normalized to their respective spectral line intensities of Nb 3d electron. The intensities of Er 4d electron (range from 160 to 180 eV) were enlarged by 10 times

After all the optical measurements, the samples were used to measure the XPS spectra. The XPS spectra are presented in Fig. 2. It is clear that the position and shape of Nb 3d electron binding energy are invariable, whereas those of Er 4d electron binding energy vary obviously. The peak binding energy of Nb 3d electron is ~206.2 eV, which is very close to the bonding energy of KNbO₃ [26], without other peak or shoulder. This indicates that the Nb element exists as the only form of NbO₃⁻¹. The peak binding energy of Er 4d electron decreases with increasing MgO con-

centration. An important finding is that bimodal structure appears for NSLN:Er:MgO(1.0) and becomes clearer for NSLN:Er:MgO(2.0). Although the specific compound corresponding to the binding energy can not be confirmed, the bimodal structure implies that there are two Er³⁺ occupational sites.

In addition, the relative concentration of each element can be obtained from their intensities in XPS spectra combining with sensitivity factors. The obtained Er element mass concentrations relative to Nb element are 1.17, 1.30, 1.76, and 2.06%, respectively. It is clear that Er³⁺ segregation coefficient increases with increasing MgO concentration in NSLN:Er:MgO. This trend agrees with the case that MgO codoping induces the increase of the Nd³⁺ distribution coefficient in CLN [27]. The corresponding molar concentrations are tabulated in Table 1.

3.2 Photorefractive damage threshold and OH⁻ absorption peak shift

Photorefractive damage in LN crystal limits its application at high power. Conventional photorefractive damage threshold is defined as the minimum power of a 532 nm CW laser at which the transmitted laser beam is elongated along the *c*-axis after 10 min of irradiation [28]. Figure 3 shows the spatial profiles of the laser beams passed through the samples with a power of 270 mW, i.e., power density of ~3.8 MW/cm². As can be seen, NSLN:Er:MgO(2.0) can withstand this power density without laser beam distortion, NSLN:Er:MgO(1.0) shows a minor beam distortion, whereas the others exhibit severe beam distortion. Minor beam distortion in NSLN:Er:MgO(1.0) implies that 1 mol% MgO is slightly low for resisting photorefractive damage. This seems inconsistent with literature [13] but by depth study we find that this inconsistency attributes to low Li concentration (49.3%) in our NSLN because the LN with higher Li concentration owns lower MgO threshold value of photorefractive damage [29]. Their corresponding photorefractive damage thresholds are listed in the last column of Table 1. As can be seen from the table, the photorefractive damage threshold of NSLN:Er:MgO(2.0) increases by about 4000 times compared with that of NSLN:Er, which is coincided with the enhancement of SLN:Mg18 compared with

Table 1 The compositions of charges, the final [Li]/[Nb] ratio and Er³⁺ concentrations in the crystals, and the photorefractive damage thresholds

Sample	[Li]/[Nb] (in melt)	K ₂ O (in melt)	Er ₂ O ₃ (in melt)	MgO (in melt)	[Li]/[Nb] (in crystal)	Er ³⁺ (in crystal)	Photorefractive damage threshold (KW/cm ²)
NSLN:Er	1.0	6 mol%	0.5 mol%	0 mol%	0.972	0.66 mol%	1.2
NSLN:Er:MgO(0.5)	1.0	6 mol%	0.5 mol%	0.5 mol%	0.972	0.74 mol%	6.8
NSLN:Er:MgO(1.0)	1.0	6 mol%	0.5 mol%	1.0 mol%	0.972	1.00 mol%	3.9 × 10 ³
NSLN:Er:MgO(2.0)	1.0	6 mol%	0.5 mol%	2.0 mol%	0.972	1.18 mol%	4.7 × 10 ³

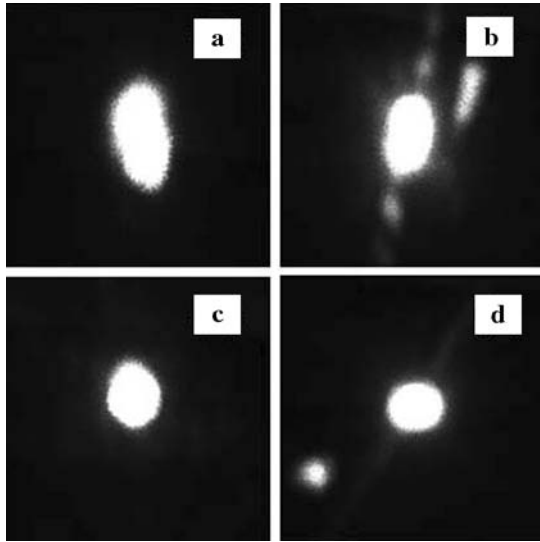


Fig. 3 Spatial profiles of the 532 nm CW frequency-doubled Nd:YAG laser beam after passing through the samples at the end of 10 min of irradiation with a power of 270 mW. The screen was at a distance of 1 m from the exit plane of the samples. (a) NSLN:Er, (b) NSLN:Er:MgO(0.5), (c) NSLN:Er:MgO(1.0), and (d) NSLN:Er:MgO(2.0)

SLN-Mg06 (~5000 times) [25]. Usually, this enhancement is explained as the increase of photoconductivity [28].

OH^- absorption feature is sensitive to some properties of LN grown in air, such as the site occupation of protons, the components of OH^- absorption bands, and its relationship with the intrinsic defects [30]. From Fig. 4 one finds that both NSLN:Er and NSLN:Er:MgO(0.5) have strong absorption peak at 3481 cm^{-1} with shoulder at 3467 cm^{-1} . Whereas for NSLN:Er:MgO(1.0) and NSLN:Er:MgO(2.0) the main absorption peak shifts to 3535 cm^{-1} . According to the results reported by Zhang [31] the absorption peak at 3535 cm^{-1} is associated with the stretching vibration of $\text{Mg}_{\text{Li}}^+ \text{OH}^- \text{Mg}_{\text{Nb}}^{3-}$ complex. OH^- absorption features of SLN, SLN:Er, and SLN:Er:MgO(1.0 mol%) were investigated by Lee et al. [32], the peak around 3489 cm^{-1} of SLN:Er, which is associated with the stretching vibration of $\text{Er}_{\text{Li}}^{2+} \text{OH}^-$ complex, does not appear in the OH^- absorption spectra of our samples because it is maybe enshrouded in the stronger peak at 3481 cm^{-1} , and the peak at around 3466 cm^{-1} of SLN appears in the OH^- absorption spectra of NSLN:Er and NSLN:Er:MgO(0.5) as shoulder. The co-existence of peaks at 3467 and 3481 cm^{-1} indicates that our LN crystal is neither congruent nor stoichiometric composition. An obvious peak shift occurs when MgO concentration reaches or exceeds 1 mol%. It is worth to emphasize that this shift is also observed in the cases of MgO- and ZnO-doped CLN crystals when the concentrations reach or exceed their threshold concentrations [33, 34]. Thus, the threshold concentration of MgO in NSLN:Er is slightly above 1 mol%.

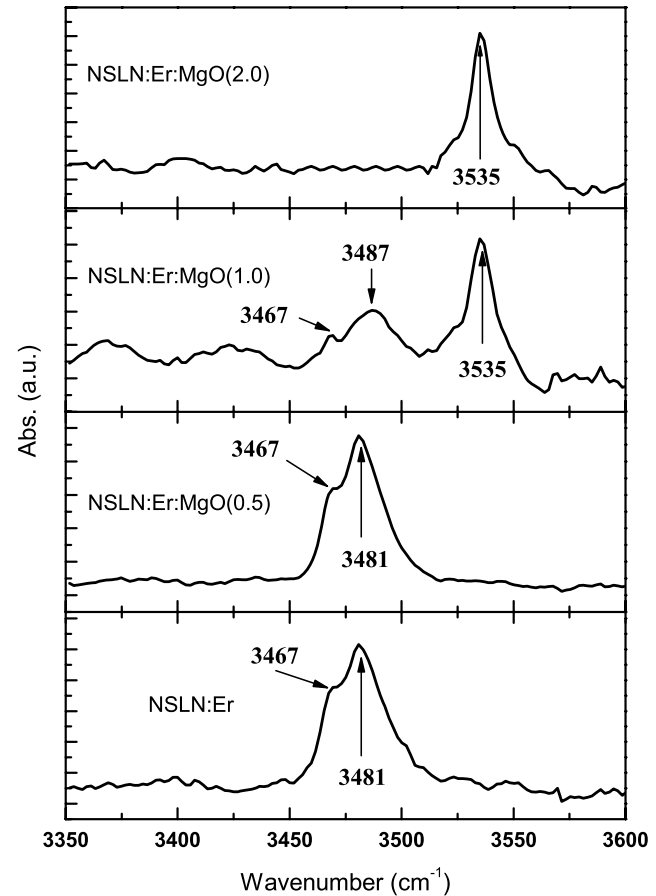


Fig. 4 OH^- absorption spectra of the four samples

This is in agreement with the measurement of photorefractive damage threshold.

3.3 Absorption spectra and spectroscopic analysis

Unpolarized absorption spectra of these four NSLN:Er:MgO crystals are shown in Fig. 5. Eleven transition bands consisted of twelve transitions can be separated in the UV-visible-IR region. JO theory has been applied to the spectroscopic investigation of Er³⁺ in single- or double-doped LN crystal [18, 35], so we only provide a short synopsis. The theoretical transition strength from level *i* to *f* can be expressed as

$$\begin{aligned} & f(i, f)_{\text{calc}} \\ &= \frac{8\pi^2 mc}{3h(2J_i + 1)\bar{\lambda}} \\ & \times \left(X_{\text{ed}} \sum_{\lambda=2,4,6} \Omega_\lambda |\langle i \parallel U^{(\lambda)} \parallel f \rangle|^2 + \frac{X_{\text{md}} S_{\text{md}}}{e^2} \right), \quad (1) \end{aligned}$$

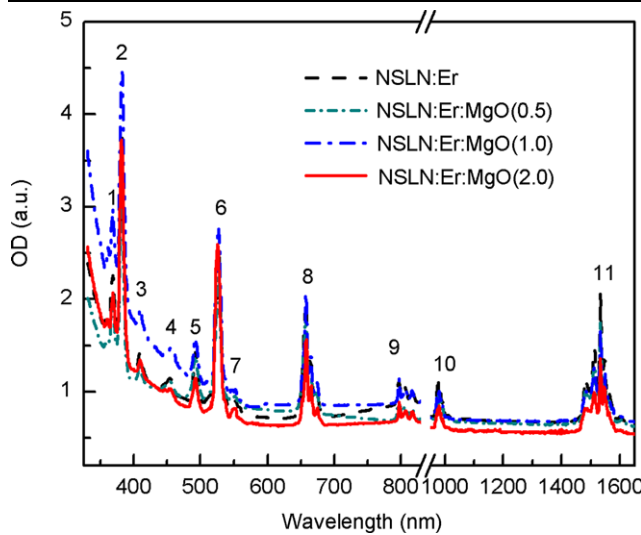


Fig. 5 Room temperature absorption spectra of the samples. The peaks ascribe to the transition (1, 2, ..., 11) from ground state ($^4I_{15/2}$) to various excited states, which are listed in the second column of Table 2

and experimental transition strength can be obtained from absorption spectrum according to

$$f(i, f)_{\text{meas}} = \frac{4m\epsilon_0 c^2}{Ne^2 d(\bar{\lambda})^2} \int \ln(10) OD(\lambda) d\lambda. \quad (2)$$

Table 2 Barycenter wavelength ($\bar{\lambda}$), predicted refractive indexes (n) based on composition-dependent Sellmeier equation, measured (f_{meas}) and calculated (f_{calc}) transition strengths (in unit of $\times 10^{-8}$),

Transition	Final states	$\bar{\lambda}$ (nm)	n_o	n_e	NSLN:Er		NSLN:Er:		NSLN:Er:		NSLN:Er:	
					f_{meas}	f_{calc}	MgO(0.5)	f_{meas}	f_{calc}	MgO(1.0)	f_{meas}	f_{calc}
1	$^4G_{9/2}$	367	2.495	2.366	868.5	729.6	571.8	507.1	555.5	427.2	296.3	256.0
2	$^4G_{11/2}$	382	2.467	2.343	2554	2537	1853	1845	1881	1838	1430	1451
3	$^2H_{9/2}$	409	2.422	2.306	240.2	181.3	164.1	140.9	134.3	92.2	93.1	57.7
4	$^4F_{3/2,5/2}$	453	2.374	2.266	205.1	187.3	161.5	151.3	145.2	89.5	62.6	57.3
5	$^4F_{7/2}$	493	2.344	2.242	409.6	561.7	352.3	420.3	228.7	301.4	146.1	185.3
6	$^2H_{11/2}$	525	2.325	2.226	1257	1293	922.5	939.6	850.8	935.7	779.2	737.8
7	$^4S_{3/2}$	549	2.313	2.216	146.5	93.1	106.7	75.2	53.4	44.8	63.6	28.4
8	$^4F_{9/2}$	660	2.279	2.187	758.2	831.6	551.1	585.2	394.2	480.5	268.3	288.8
9	$^4I_{9/2}$	806	2.254	2.167	132.6	177.9	98.7	121.2	64.0	106.5	43.9	63.4
10	$^4I_{11/2}$	981	2.237	2.152	158.4	99.7	109.7	80.0	76.4	52.6	58.2	36.6
11	$^4I_{13/2}$	1522	2.209	2.129	384.6	266.8	255.0	207.5	164.0	137.7	89.8	87.4
					$\Omega_2 = 2.49$		$\Omega_2 = 1.94$		$\Omega_2 = 2.21$		$\Omega_2 = 2.10$	
					$\Omega_4 = 5.04$		$\Omega_4 = 3.43$		$\Omega_4 = 3.03$		$\Omega_4 = 1.81$	
					$\Omega_6 = 1.37$		$\Omega_6 = 1.11$		$\Omega_6 = 0.66$		$\Omega_6 = 0.42$	
					$\delta_{\text{rms}} = 89$		$\delta_{\text{rms}} = 42$		$\delta_{\text{rms}} = 77$		$\delta_{\text{rms}} = 42$	

The meanings of all symbols above can refer to [36]. $\Omega_\lambda (\lambda = 2, 4, 6)$ can be extracted when the theoretical transition strengths given by (1) are fitted to the experimental ones given by (2) using least-squares fitting. The accuracy of the fitting between the experimental and calculated oscillator strengths is given by the root mean-square deviation (δ_{rms}). Ω_λ and δ_{rms} , as well as f_{meas} and f_{calc} , are listed in Table 2.

LN crystal is an uniaxial crystal, which is anisotropic, so polarized absorption spectra should be used to insure the validity of JO intensity parameters. But Núñez's research on polarization effect in LN indicates that the values of Ω_4 and Ω_6 obtained from the unpolarized absorption spectrum of a Y -cut sample are close to the values of effective Ω_4 and Ω_6 obtained on an average of σ - and π -polarized absorption spectra, though the values of Ω_2 are very different in these two cases [37]. So in this paper we mainly give attention to Ω_4 and Ω_6 . Compared with CLN:Er [18], although the value of Ω_6 remains invariant, the value of Ω_4 largens greatly in NSLN:Er. The values of Ω_4 and Ω_6 decrease gradually with increasing MgO concentration. Although the values of Ω_2 are not creditable, the change trend should be creditable. We think that MgO codoping has very limited influence on Ω_2 in our NSLN:Er:MgO crystal series because the value of Ω_2 is uneven and non-monotonic.

and JO intensity parameters (Ω) (in unit of $\times 10^{-20} \text{ cm}^2$) of Er³⁺ in NSLN:Er:MgO crystals at 300 K. Root mean square deviation (δ_{rms}) (in unit of $\times 10^{-8}$) is also listed in the last row.

Table 3 Radiative decay rates (A), fluorescence branching ratios (β), and peak stimulated emission cross section (σ) for concerned green and 1.54- μm transitions

	NSLN:Er	NSLN:Er:MgO(0.5)	NSLN:Er:MgO(1.0)	NSLN:Er:MgO(2.0)
$^4S_{3/2} \rightarrow ^4I_{15/2}$				
$A (\text{s}^{-1})$	4330	3495	2676	1316
β	0.683	0.686	0.685	0.681
$\sigma (\times 10^{-21} \text{cm}^2)$	9.3	7.5	5.4	2.8
$^4I_{13/2} \rightarrow ^4I_{15/2}$				
$A (\text{s}^{-1})$	533	439	328	248
β	1	1	1	1
$\sigma (\times 10^{-21} \text{cm}^2)$	9.4	6.7	4.5	3.1

After JO intensity parameters are known, radiative decay rate (A_{if}) can be calculated according to

$$A_{if} = \frac{16\pi^3 n^2}{3h\varepsilon_0(2J_i + 1)(\bar{\lambda})^3} \times \left(e^2 X_{\text{ed}} \sum_{\lambda=2,4,6} \Omega_\lambda |\langle i \parallel U^{(\lambda)} \parallel f \rangle|^2 + X_{\text{md}} S_{\text{md}} \right). \quad (3)$$

The fluorescence branching ratio (β) is given by

$$\beta(i, f) = \frac{A_{if}}{\sum_m A_{im}}, \quad (4)$$

where the summation is carried out over all lower-lying energy levels (m).

The peak stimulated emission cross section is defined as

$$\sigma_{if} = \frac{\lambda^4 A_{if}}{4\pi^2 c n^2 \Delta\lambda_{\text{eff}}}, \quad (5)$$

where λ is the peak wavelength, and $\Delta\lambda_{\text{eff}}$ is the effective linewidth.

From Table 3, one can clearly see that the peak stimulated emission cross section decreases with increasing MgO concentration. The peak stimulated emission cross section at 550.7 nm in NSLN:Er:MgO(1.0) crystal equals to that in CLN:Er:Sc₂O₃ crystal fiber ($5.4 \times 10^{-21} \text{cm}^2$) [38]. This implies that NSLN:Er:MgO(1.0) with enhanced photorefractive damage threshold is suitable for fiber upconversion (UC) laser around 550 nm. The peak stimulated emission cross section at 1532 nm in NSLN:Er:MgO(1.0), which is calculated using the McCumber relation [39], is comparable to that in YAG:Er ($5 \times 10^{-21} \text{cm}^2$) [40] in which lasing action has been actualized at room temperature. High fluorescence branching ratios mean high laser conversion efficiencies for these two potential laser transitions.

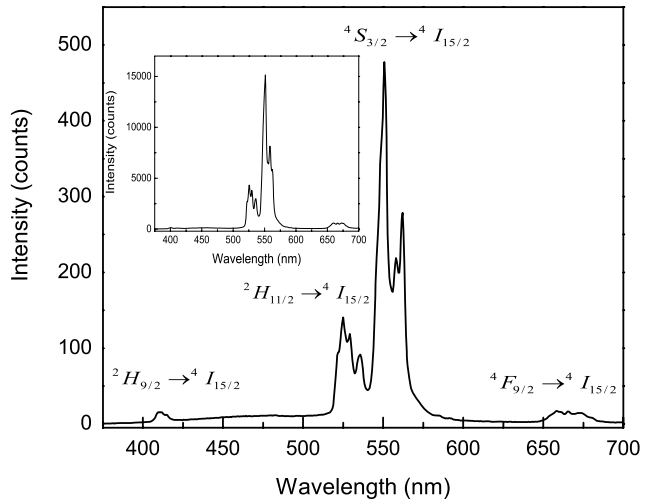


Fig. 6 UC visible emission spectrum of NSLN:Er:MgO(1.0) obtained with 2- μs gate and 140-ns delay. The emission bands are assigned in figure. Inset is the corresponding spectrum obtained with 990- μs gate and 11-ns delay

3.4 Upconversion emission spectra and excitation mechanism

Green luminescence is observed by naked eyes under 800-nm near-IR laser excitation, the UC emission spectrum of NSLN:Er:MgO(1.0) is displayed in Fig. 6. A gate delay in time-resolved spectroscopy is used in order to gate out the undesirable second-harmonic wave and supercontinuous white lights generated by self-phase modulation under femtosecond laser irradiation [41]. Four transition bands are observed in the spectrum with an acquisition time of 2 μs . The violet band (~ 410 nm) becomes indistinct in the spectrum with an acquisition time of 990 μs (see insert of Fig. 6). This decrease of relative intensity is caused by short lifetime of $^2H_{9/2}$ state compared with these of $^4S_{3/2}$ and $^4F_{9/2}$ states.

The green emission bands with better resolution are shown in Fig. 7. The most important difference is the appearance of a new shoulder at 562.6 nm in the emission spectrum of NSLN:Er:MgO(2.0), which is marked with as-

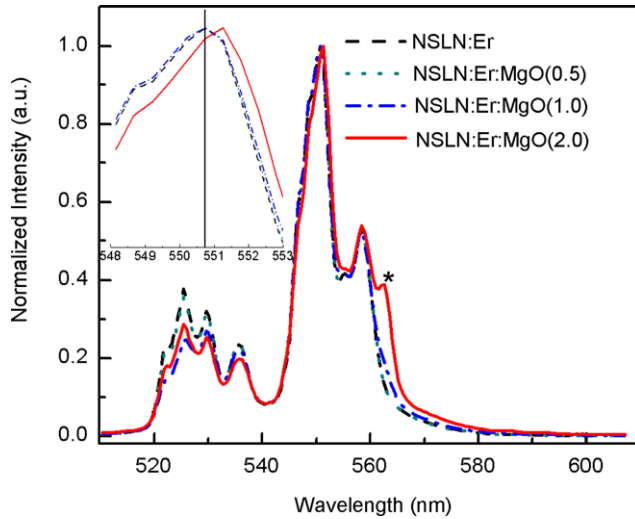


Fig. 7 The enlarged emission spectra between 510 and 610 nm obtained with gate width of 990 μs and with gate delay of 115 ns. The spectra are normalized to their respective maxima. Inset shows the peak shift of their maxima

terisk. New shoulder is also observed in the emission spectra of CLN:Er:MgO(6.0) and CLN:Er:MgO(8.0) [21] but it is more obvious for NSLN:Er:MgO(2.0). The new shoulder is also assigned to the Er³⁺ in a crystal-field site modified by a Mg²⁺ inclusion as we did in [21]. The other finding is that the emission peak of NSLN:Er:MgO(2.0) redshifts by 0.5 nm compared with the others, as shown in the inset of Fig. 7. This redshift implies that the covalence degree of Er³⁺-ligand bonds is enhanced [42] so the Er³⁺ local environment is changed after introducing 2 mol% MgO into NSLN:Er. The spectral resolution is only 0.5 nm in our experiments, and a higher spectral resolution is needed for the systematical investigation of peak shift.

Population distribution between $^2H_{11/2}$ and $^4S_{3/2}$ states satisfies thermal equilibrium condition, so their luminescent intensity ratio ($I_{^2H_{11/2}}/I_{^4S_{3/2}}$) is related to the temperature of luminescent point [43] and their ratio values are 0.43, 0.42, 0.34, and 0.32, respectively. So energy dissipation in the crystal decreases with increasing MgO concentration, i.e., with increasing Er³⁺ concentration. Higher Er³⁺ concentration with lower energy dissipation is unexpected, and this phenomenon may attribute to the increase of cross relaxation (CR) of $^4S_{3/2} + ^4I_{15/2} \rightarrow ^4I_{9/2} + ^4I_{13/2}$ which absorbs phonons in YAlO₃:Er [44].

Time-resolved emission spectra obtained at two different delay times are shown in Fig. 8. For NSLN:Er and NSLN:Er:MgO(0.5), although the intensities at the end of decay are much lower, the shapes are essentially the same as these in the early stage of decay. However, a difference in the shape appears when codoping with MgO reaches 1 mol% and becomes more obvious when codoping with MgO reaches 2 mol%. In time-resolved spectroscopy, rare earth ions located in different crystal-field sites will lead to

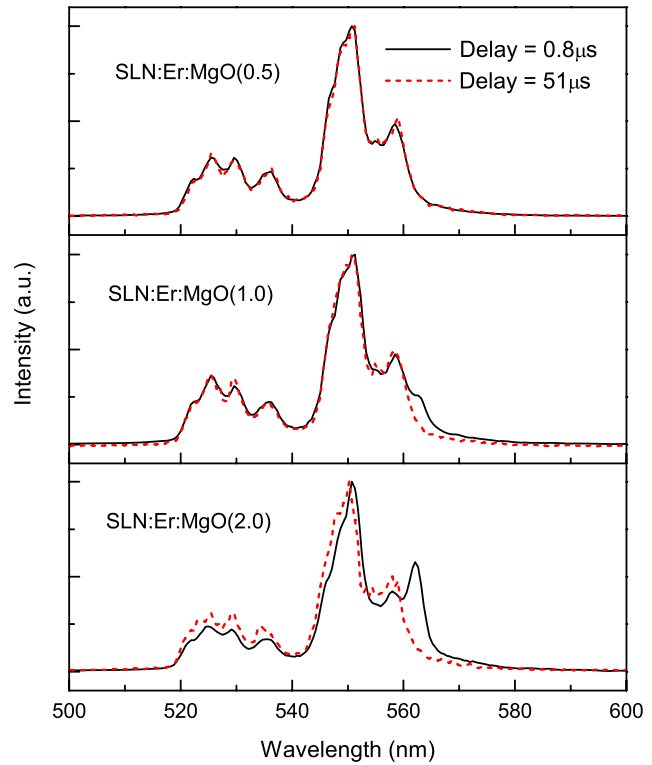


Fig. 8 Normalized time-resolved emission spectra obtained with 0.5- μs gate width and delay of 0.8 and 51 μs after excitation pulse

a difference in the shape of emission spectra obtained at different delay time [45]. Above result implies that all Er³⁺ ions are located at a similar crystal-field site in NSLN:Er and NSLN:Er:MgO(0.5), and a new crystal-field site comes forth when codoping with MgO reaches 1 mol%. These coincide with the bimodal structure in XPS spectra (see Fig. 2) in NSLN:Er:MgO(1.0) and NSLN:Er:MgO(2.0). It can therefore be concluded that mildly MgO codoping has limited influence on the crystal-field site of Er³⁺, whereas heavily MgO codoping will induce a new crystal-field site.

To understand the UC excitation mechanism, the pump energy dependence of the fluorescent intensity is investigated. For an unsaturated UC process, the number of the photons required to populate the upper emitting state can be calculated by [46]

$$I_{\text{UC}} \propto P^n, \quad (6)$$

where I_{UC} is the UC emission integrated intensity, P is the incident pump laser energy, and n is the number of the laser photon required to emit a higher energy visible photon. The pump energy dependencies of UC emission intensities are plotted in Fig. 9, n equals to the slope of the graph of $\ln(I_{\text{UC}})$ versus $\ln(P)$. All slopes are close to 2.5, and the half integer is ascribed to the effect of self-focusing [47] instead of CR [48]. All the concerned UC emission bands exhibit approx-

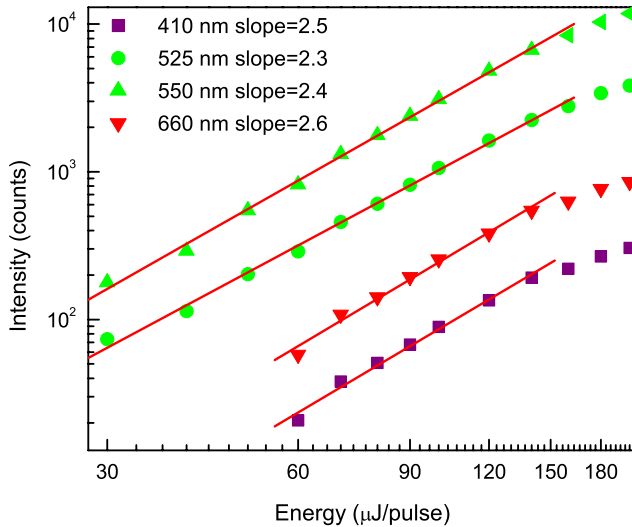


Fig. 9 Double logarithmic plot of the pump energy dependence of the UC emission intensities. The errors of slope are less than 0.1

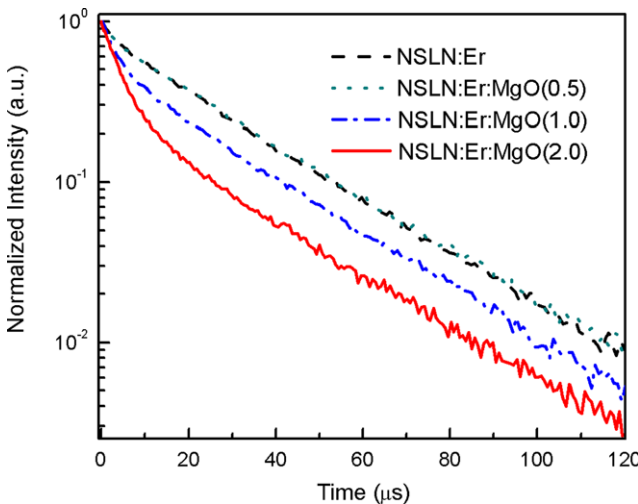


Fig. 10 Semilogarithmic plot of the decay curves of Er^{3+} at 550 nm in these samples after 800-nm pulse excitation

imately quadratic power law versus pump energy indicating that these UC emissions are two-photon processes.

800-nm photon is resonant with ${}^4I_{9/2}$ level, so excited state absorption (ESA) or energy transfer UC (ETU) is operative. ETU and ESA can be distinguished by decay kinetics [49]: If there is a delay in excitation, it is ETU, otherwise it is ESA. There is no rise stage in the decay curve of Fig. 10, so ESA is dominant.

The positions of energy levels for Er^{3+} in LN crystal are obtained from literature [50]. The laser photon energy is $\sim 12500 \text{ cm}^{-1}$, which is resonant or quasiresonant with the ground state absorption (GSA) (${}^4I_{15/2} \rightarrow {}^4I_{9/2}$) and three ESAs (${}^4I_{9/2} \rightarrow {}^2H_{9/2}$, ${}^4I_{11/2} \rightarrow {}^4F_{3/2}$, and ${}^4I_{13/2} \rightarrow {}^2H_{11/2}$). Synthetically considering the strengths of transition, the lifetimes of excited state, and the pulse duration

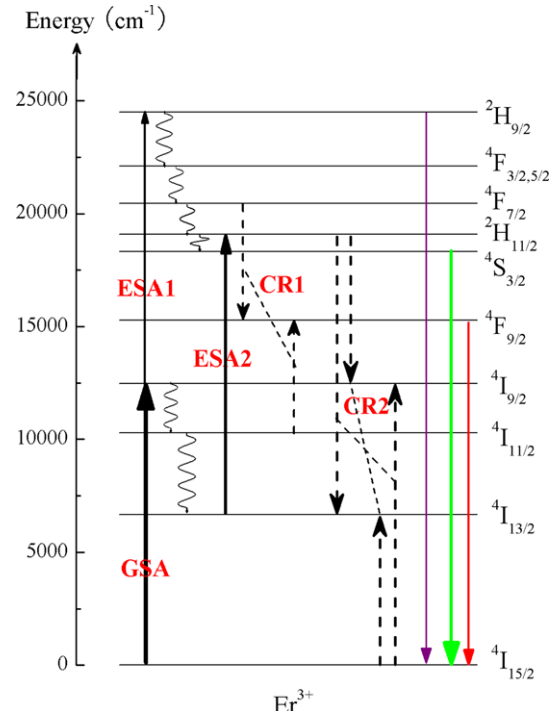


Fig. 11 Schematic energy level diagrams of Er^{3+} in LN crystal, and UC excitation and visible emission schemes. The solid, dotted, and wavy arrows denote radiative transition, CR, and multiphonon relaxation, respectively

and repetition rate of the pump laser, the third ESA owns the highest pump efficiency, whereas the second ESA is hardly operative. Based on above discussion, we proposed the following UC processes, which are represented in Fig. 11. The green luminescence mainly originates from GSA/ESA2, and the violet emission only originates from GSA/ESA1. The operative way of GSA/ESA2 has been reported under femtosecond laser excitation [51]. There is no ESA terminating at ${}^4F_{9/2}$ level which makes the origin of red emission difficult to identify. If ${}^4F_{9/2}$ state is mainly fed from ${}^4S_{3/2}$ level, a rise stage should be exhibited in the decay curves at 660 nm [52]. The absence of a rise stage in this decay curve excludes the feeding from ${}^4S_{3/2}$ level, and feeding from ${}^4F_{7/2}$ by CR1 (${}^4F_{7/2} + {}^4I_{11/2} \rightarrow {}^4F_{9/2} + {}^4F_{9/2}$) is adopted. The populations at ${}^2H_{9/2}$ rapidly relax to ${}^4F_{7/2}$ via multiphonon relaxation, and ${}^4F_{7/2}$ state is a very short-lived state because the multiphonon relaxation is effective. Short-lived ${}^4F_{7/2}$ state, which is an initial states of CR1, also explains that the intensity of red luminescence is low. Namely, the red emission originates from GSA/ESA1/CR1.

3.5 The distribution of Er^{3+} -clustered sites

The energy of ${}^2H_{11/2}$ excited state, which is thermally coupled with ${}^4S_{3/2}$ state, equals to the energy sum of ${}^4I_{9/2}$ and ${}^4I_{13/2}$ states in Er^{3+} -doped system. Thus if there are

Table 4 The lifetimes of isolated (τ_i) and clustered sites Er³⁺ (τ_c), and their ratios obtained using (7) and from Fig. 10

Samples	τ_i (μs)	τ_c (μs)	B/A
NSLN:Er	25.0	3.3	0.25
NSLN:Er:MgO(0.5)	25.4	2.7	0.23
NSLN:Er:MgO(1.0)	24.4	3.2	0.84
NSLN:Er:MgO(2.0)	25.1	4.2	2.72

ion pairs, i.e., clustered sites of Er³⁺, effective CRs between them will occur. The decay time of $^2H_{11/2}$ state will shorten if CR2 ($^2H_{11/2} + ^4I_{15/2} \rightarrow ^4I_{9/2} + ^4I_{13/2}$ and $^2H_{11/2} + ^4I_{15/2} \rightarrow ^4I_{13/2} + ^4I_{9/2}$) occurs and so does $^4S_{3/2}$ state [19]. So the shortening of $^4S_{3/2}$ state decay time is indicative of the existence of clustered sites. From the decay curves at 550 nm plotted in Fig. 10, accelerated decay is clearly seen in the early stage of decay curves, especially for NSLN:Er:MgO(1.0) and NSLN:Er:MgO(2.0).

According to [19], the measured nonexponential decay can be fitted to

$$I(t) = A \cdot \exp\left(-\frac{t}{\tau_i}\right) + B \cdot \exp\left(-\frac{t}{\tau_c}\right) + I_0, \quad (7)$$

where the first term is the contribution from isolated Er³⁺ with a lifetime of τ_i , the second term is the contribution from the clustered sites of Er³⁺ that involves CR2 with a lifetime of τ_c , and the last term is a time independent background noise. The fitting parameters are listed in Table 4. Except for τ_c in NSLN:Er:MgO(2.0), τ_i and τ_c coincide with Ju's results in CLN:Er [19]. B/A ratio expresses the initial population concentration of clustered sites in $^4S_{3/2}$ state. Provided that the Er³⁺ ions at clustered and isolated sites possess the same pump probability, B/A ratio is also proportional to the concentration of Er³⁺ at clustered sites. So we can conclude that: (1) The lifetime of isolated Er³⁺ is ~25 μs, and that of clustered sites Er³⁺ is ~3 μs, moreover they are both independent of Li/Nb ratio and of the concentration of codopant. (2) MgO codoping under 1.0 mol% in NSLN:Er has very limited influence on clustering, whereas MgO codoping up to or above 1 mol% facilitates the formation of Er³⁺-clustered sites. The latter conclusion coincides with the IR absorption measurements. Mg_{Li}⁺-OH-Mg_{Nb}³⁻ complex, which is confirmed by the absorption peak at 3535 cm⁻¹, indicates that Mg²⁺ ions in NSLN:Er:MgO(1.0) and NSLN:Er:MgO(2.0) occupy almost all Li⁺ sites and start to occupy Nb⁵⁺ sites, and evict partial Er³⁺ original inhabited Li⁺ sites into Nb⁵⁺ sites, namely, induce the formation of Er_{Nb}²⁻, and the pair of Er_{Li}²⁺ and Er_{Nb}²⁻ with short distance is so-called clustered site of Er³⁺. The influence of MgO codoping on clustering in NSLN:Er:MgO is similar to that in CLN:Er:MgO [21] but the influence in NSLN:Er:MgO is slighter. Clustered

sites of Er³⁺ is deleterious to the application at 1.5 μm, so NSLN:Er:MgO is more suitable than CLN:Er:MgO for potential application in the field of optical communications.

4 Conclusions

The [Li]/[Nb] ratio of 0.972 is obtained in NSLN:Er grown from K₂O-based flux using top seeded solution growth technique, and MgO codoping facilitates the incorporation of Er³⁺ into NSLN. Codoping 1 mol% or more MgO into NSLN:Er can enhance photorefractive damage threshold by three orders of magnitude. The values of Ω_4 and Ω_6 decrease gradually with increasing MgO concentration, whereas MgO codoping has very limited influence on the value of Ω_2 . MgO codoping up to 2 mol% not only can enhance the covalence degree of the Er³⁺-ligand bonds, but also can induce a new Er³⁺ crystal-field site. The green UC emission comes mainly from GSA/ESA of $^4I_{13/2} \rightarrow ^2H_{11/2}$, the emission at 410 nm only originates from GSA/ESA of $^4I_{9/2} \rightarrow ^2H_{9/2}$, whereas the red emission ascribes to CR of $^4F_{7/2} + ^4I_{11/2} \rightarrow ^4F_{9/2} + ^4F_{9/2}$. Slightly MgO codoping (under 1 mol%) has very limited influence on the clustering, whereas heavily MgO codoping (up to and above 1 mol%) facilitates the formation of Er³⁺ clustered sites in NSLN. NSLN:Er:MgO(1.0) is the most suitable candidate for amplifiers and fiber lasers around 1.5 μm among these samples due to the high photorefractive damage threshold, moderate peak stimulated emission cross section, and proper Er³⁺-clustered sites concentration.

Acknowledgements This work was partially supported by National Natural Science Foundation of China (Grant No. 10774034).

References

1. D. Janner, D. Tulli, M. García-Granda, M. Belmonte, V. Pruneri, *Laser Photonics. Rev.* **3**, 301 (2009)
2. D.G. Lim, B.S. Jang, S.I. Moon, C.Y. Won, J. Yi, *Solid State Electron.* **45**, 1159 (2001)
3. S.K.R.S. Sankaranarayanan, V.R. Bhethanabotla, *IEEE Sens. J.* **9**, 329 (2009)
4. J.Q. Sun, H. Li, Y.S. Cheng, J.L. Li, *Opt. Commun.* **281**, 5874 (2008)
5. I. Baumann, S. Bosso, R. Brinkmann, R. Corsini, M. Dinand, A. Greiner, K. Schäfer, J. Söchtig, W. Sohler, H. Suche, R. Wessel, *IEEE J. Sel. Top. Quantum Electron.* **2**, 355 (1996)
6. Y.L. Chen, J. Guo, C.B. Lou, J.W. Yuan, W.L. Zhang, S.L. Chen, Z.H. Hung, G.Y. Zhang, *J. Cryst. Growth* **263**, 427 (2004)
7. T.R. Volk, N.M. Rubinina, *Opt. Lett.* **15**, 996 (1990)
8. T.R. Volk, N.M. Rubinina, *Ferroelectr. Lett. Sect.* **14**, 37 (1992)
9. J.K. Yamamoto, N.K.K. Iyi, S. Kimura, *Appl. Phys. Lett.* **61**, 2156 (1992)
10. E.P. Kokanyan, L. Razzari, I. Cristiani, V. Degiorgio, J.B. Gruber, *Appl. Phys. Lett.* **84**, 1880 (2004)
11. L.F. Johnson, A.A. Ballman, *J. Appl. Phys.* **40**, 297 (1969)

12. E. Montoya, J. Capmany, L.E. Bausá, T. Kellner, A. Diening, G. Huber, *Appl. Phys. Lett.* **74**, 3113 (1999)
13. M. Nakamura, S. Higuchi, S. Takekawa, K. Terabe, Y. Furukawa, K. Kitamura, *Jpn. J. Appl. Phys.* **41**, L49 (2002)
14. Y. Furukawa, K. Kitamura, S. Takekawa, A. Miyamoto, M. Terao, N. Suda, *Appl. Phys. Lett.* **77**, 2494 (2000)
15. D. Xue, K. Betzler, *Appl. Phys. B* **72**, 641 (2001)
16. B.R. Judd, *Phys. Rev.* **127**, 750 (1962)
17. G.S. Ofelt, *J. Chem. Phys.* **37**, 511 (1962)
18. J. Amin, B. Dussardier, T. Schweizer, M. Hempstead, *J. Lumin.* **69**, 17 (1996)
19. J.J. Ju, M.H. Lee, M. Cha, H.J. Seo, *J. Opt. Soc. Am. B* **20**, 1990 (2003)
20. A.H. Li, L. Sun, Z.R. Zheng, W.Z. Wu, W.L. Liu, Y.Q. Yang, T.Q. Lü, W.H. Su, *J. Lumin.* **128**, 239 (2008)
21. A.H. Li, Z.R. Zheng, L. Sun, Q. Lü, W.L. Liu, W.Z. Wu, Y.Q. Yang, T.Q. Lü, *J. Appl. Phys.* **104**, 033511 (2008)
22. S. Solanki, T.C. Chong, X.W. Xu, *J. Cryst. Growth* **250**, 134 (2003)
23. G. Dravecz, Á. Péter, K. Polgár, L. Kovács, *J. Cryst. Growth* **286**, 334 (2006)
24. L. Kovács, G. Ruschhaupt, K. Polgár, G. Corradi, M. Wöhlecke, *Appl. Phys. Lett.* **70**, 2801 (1997)
25. K. Niwa, Y. Furukawa, S. Takekawa, K. Kitamura, *J. Cryst. Growth* **208**, 493 (2000)
26. C.D. Wagner, W.M. Riggs, L.E. Davis, J.F. Moulder, *Handbook of X-Ray Photoelectron Spectroscopy* (Perkin-Elmer Corporation, 1979)
27. K.G. Belabaev, A.A. Kaminskii, S.E. Sarkisov, *Phys. Status Solidi (a)* **28**, K17 (1975)
28. J.N.B. Reddy, K.G. Kamath, S. Vanishri, H.L. Bhat, S. Elizabeth, *J. Chem. Phys.* **128**, 244709 (2008)
29. Y. Furukawa, K. Kitamura, S. Takekawa, A. Miyamoto, M. Terao, N. Suda, *Appl. Phys. Lett.* **77**, 2494 (2000)
30. Y.F. Kong, W.L. Zhang, X.J. Chen, J.J. Xu, G.Y. Zhang, *J. Phys., Condens. Matter* **11**, 2139 (1999)
31. D.L. Zhang, D.C. Wang, E.Y.B. Pun, *J. Appl. Phys.* **97**, 103524 (2005)
32. S.M. Lee, T.I. Shin, Y.T. Kim, M. Habu, T. Ito, M. Natori, D.H. Yoon, *Mater. Sci. Eng. B* **105**, 34 (2003)
33. D.A. Bryan, R. Gerson, H.E. Tomaschke, *Appl. Phys. Lett.* **44**, 847 (1984)
34. Y. Zhang, Y.H. Xu, M.H. Li, Y.Q. Zhao, *J. Cryst. Growth* **233**, 537 (2001)
35. D.L. Zhang, Y.H.H.P.R. Xu, E.Y.B. Pun, *J. Appl. Phys.* **101**, 053523 (2007)
36. A. Li, L. Sun, Z. Zheng, Q. Lü, W. Wu, W. Liu, Y. Yang, T. Lü, *Appl. Phys. B* **90**, 29 (2008)
37. L. Núñez, G. Lifante, F. Cussó, *Appl. Phys. B* **62**, 485 (1996)
38. R. Burlot, R. Moncorgé, G. Boulon, *J. Lumin.* **7274**, 135 (1997)
39. D.E. McCumber, *Phys. Rev.* **136**, A954 (1964)
40. H. Stange, K. Petermann, G. Huber, E.W. Duczynski, *Appl. Phys. B* **49**, 269 (1989)
41. O.M. Efimov, K. Gabel, L.B. Glebov, S. Grantham, M. Richardson, M.J. Soileau, *J. Opt. Soc. Am. B* **15**, 193 (1998)
42. M. Ajroud, M. Haouari, H.B. Ouada, H. Maaref, A. Brenier, C. Garapon, *J. Phys., Condens. Matter* **12**, 3181 (2000)
43. T. Hayakawa, M. Hayakawa, M. Nogami, *J. Alloys Compd.* **451**, 77 (2008)
44. J. Breguet, A.F. Umyakov, S.G. Semenkov, W. Lüthy, H.P. Weber, I.A. Shcherbakov, *IEEE J. Quantum Electron.* **28**, 2563 (1992)
45. J.W. Stouwdam, G.A. Hebbink, J. Huskens, F.C.J.M. van Veggel, *Chem. Mater.* **15**, 4604 (2003)
46. F. Pandozzi, F. Vetrone, J. Boyer, R. Naccache, J.A. Capobianco, A. Speghini, M. Bettinelli, *J. Phys. Chem. B* **109**, 17400 (2005)
47. A.H. Li, Q. Lü, Z.R. Zheng, L. Sun, W.Z. Wu, W.L. Liu, H.Z. Chen, Y.Q. Yang, T.Q. Lü, *Opt. Lett.* **33**, 693 (2008)
48. X.X. Luo, W.H. Cao, *Sci. China Ser. B* **50**, 505 (2007)
49. A.J. Garcia-Adeva, R. Balda, J. Fernández, E.E. Nyein, U. Hömerich, *Phys. Rev. B* **72**, 165116 (2005)
50. J.B. Gruber, D.K. Sardar, R.M. Yow, B. Zandi, E.P. Kokanyan, *Phys. Rev. B* **69**, 195103 (2004)
51. T. Hayakawa, M. Hayakawa, M. Nogami, *J. Ceram. Soc. Jpn.* **116**, 1092 (2008)
52. J. Rubin, A. Brenier, R. Moncorge, C. Pedrini, *J. Lumin.* **36**, 39 (1986)